metals

MDPI

Article

Effect of Heat Treatment on the Microstructure and Hardness of Ni-Based Alloy 718 in a Variable Thickness Geometry Deposited by Powder Fed Directed Energy Deposition

Pedro Ramiro [1,*], Haize Galarraga [1], Anabel Pérez-Checa [1], Mikel Ortiz [1], Amaia Alberdi [1], Trunal Bhujangrao [1], Elena Morales [1] and Eneko Ukar [2]

[1] TECNALIA, Basque Research and Technology Alliance (BRTA), Paseo Mikeletegi 2 and 7, 20009 Donostia-San Sebastian, Spain; haize.galarraga@tecnalia.com (H.G.); anabel.perez@tecnalia.com (A.P.-C.); mikel.ortiz@tecnalia.com (M.O.); amaia.alberdi@tecnalia.com (A.A.); trunal.bhujangrao@tecnalia.com (T.B.); elena.morales@tecnalia.com (E.M.)

[2] Department of Mechanical Engineering, Faculty of Engineering of Bilbao, University of Basque Country, Alameda de Urquijo s/n, 48013 Bilbao, Spain; eneko.ukar@ehu.es

* Correspondence: pedro.ramiro@tecnalia.com

Abstract: Feature addition to existing parts is a trending application for Directed Energy Deposition (DED) and can be used to add complex geometry features to basic forged geometries with the aim to reduce and simplify the number of processing steps as machining and assembling. However, the mechanical properties of as-deposited Inconel 718 fabricated by Powder-fed Directed Energy Deposition (Powder-fed DED) are far lower than the relevant specifications, making it necessary to apply different heat treatment with the purpose of improving deposited material performance. In addition, the effects of heat treatments in both variable thickness deposited geometry and forge substrate have not been studied. In this study, the effect of heat treatment within the Aerospace Materials Specifications (AMS) for cast and wrought Inconel 718 on the microstructure and hardness of both the Ni-Based Alloy 718 deposited geometry and substrate are analyzed in different parts of the geometry. The microstructure of all samples (as-deposited and heat-treated) is analyzed by Scanning Electron Microscope (SEM) and Energy Dispersive Spectrometer (EDS), confirming the formation of aluminum oxides and titanium nitrides and carbonitrides in the deposited structure.

Keywords: directed energy deposition; powder; heat treatment; microstructure; alloy 718; additive manufacturing

Citation: Ramiro, P.; Galarraga, H.; Pérez-Checa, A.; Ortiz, M.; Alberdi, A.; Bhujangrao, T.; Morales, E.; Ukar, E. Effect of Heat Treatment on the Microstructure and Hardness of Ni-Based Alloy 718 in a Variable Thickness Geometry Deposited by Powder Fed Directed Energy Deposition. *Metals* **2022**, *12*, 952. https://doi.org/10.3390/met12060952

Academic Editors: Joel Andersson and Pavel Krakhmalev

Received: 10 May 2022
Accepted: 29 May 2022
Published: 31 May 2022

1. Introduction

Industrial-scale additive manufacturing, or 3D printing, has been presented as a new paradigm for manufacturing due to the possibility of fabricating a whole geometry depositing material layer upon layer, in precise geometric shapes [1].

Powder-fed Directed Energy Deposition (DED) is an AM technology that can be used to fabricate parts. However, this technique is generally used for repairing or to add material and features to existing components [2]. Therefore, applications for powder-fed DED fall into four categories: near-net-shape parts manufacturing, feature additions, coatings, and repairing.

Due to the relatively low Mass Deposition Rate (MDR) obtained with this technique, the fabrication of Near-Net-Shape Parts by powder fed DED is employed for applications where conventional manufacturing is expensive or slow. In previous works [3–5], MDRs within a range of 0.5 kg·h^{-1} to 1 kg·h^{-1} were obtained employing 3 kW laser equipment. Zhong et al. [6,7] and Li et al. [8] have shown that MDRs up to 2 kg·h^{-1} can be obtained at higher laser power on high deposition rate DED. However, the powder-fed DED MDR range results in long production cycles and higher manufacturing costs for larger parts, limiting this application to the production of low quantities and small components.

The improvement of wear properties by DED deposited coatings is another application for powder-fed DED that is gaining notoriety in current or ongoing research, i.e., Lu et al. [9] and Foster et al. [10], improved wear properties of an H13 tool steel die, Ding et al. [11] worked on controlling valve seat sealing surfaces, and Stoffel et al. [12] studied agricultural blades and machine parts coatings by DED. Furthermore, the highest MDR can be obtained in this application combining DED coating process with additional energy sources and unidirectional deposition on revolution geometries. This approach allows to increase sharply MDR, reaching 18 $kg{\cdot}h^{-1}$ at 9 kW laser power with induction assistance, as reported by Nowotny et al. [13] or by Tuominen et al. [14] at 15 kW laser power.

On the other hand, repairing by DED provides high levels of control and repeatability since it is an automated process. This process can be used for applications such as regeneration of damaged impeller blades, as reported by Lei et al. [15], or turbine blades as, studied in the work by Kaierle et al. [16].

Feature addition to existing parts is also a trending application for DED and can be used to add structural or functional elements with the aim to reduce and simplify the number of processing steps as machining and assembling. This approach also allows to combine different manufacturing techniques. Material can be deposited on any freeform substrate creating new manufacturing routes (Merklein et al. [17]) and it offers an improved product design, time saving and cost reductions. This application can support traditional process chains and enables more resource-efficient production by adding complex geometry features on basic forged geometries as did Meiners et al. for aerospace components of Ti-6Al-4V [18] or as Stadfeld proposed with his patented solution for gear teeth additive manufacturing [19]. However, microstructures and tensile properties of deposited materials are different to those resulting from conventional cast and wrought manufacturing processes due to the rapid solidification rate and thermal gradients associated to DED additive manufacturing processes. Therefore, these features need to be enhanced, applying different heat treatments after the deposition stage.

Convenience or must of after-deposition heat treatment depends on the use of the DED. Usually, coatings produced depositing materials with excellent wear properties over less resistant substrates do not need any heat treatment (Xu et al. [20]), unlike other applications where DED parts have lower mechanical properties than the specifications, e.g., material presents an anisotropic tensile behavior (Carroll et al. [21]), lower elongation values (Roy et al. [22] and Ostra et al. [23]), and lower fatigue strength (Chew et al. [24] and Zhao et al. [25]). Furthermore, in the case of feature addition application, microstructures obtained applying standard heat treatment methods both in the additively deposited material and in conventionally fabricated substrate must be investigated.

Nickel-based superalloy, chemically equivalent to Inconel 718, widely used in the aircraft engine industry, has been employed in the present work. Other applications of these alloys are found in chemical and petrochemical plants (vessels, pumps, valves, piping), power plants (industrial gas turbines), submarines (propeller blades, quick-disconnect fittings, auxiliary propulsion motors), nuclear reactors (heat-exchanger tubing, fittings), oil & gas industry (downhole tubulars, well-head hardware, flare booms) and cryogenic storage tanks. Conventional post-processing heat treatments for Inconel 718 superalloy, include a homogenization step to transform the typical columnar grains obtained in the deposited material by DED into equiaxed grains by recrystallization. This step aims to eliminate the typical material anisotropy due to direction dependent mechanical properties [23] or property alterations between different regions of the structure [8]. Heat treatment could be completed with two subsequent steps: solution treating to dissolve detrimental phases and precipitation treating in the γ matrix to bring out desirable strengthening phases, as γ' phase ($Ni_3(Al,Ti)$) and γ'' phase (Ni_3Nb), as studied by Qi et al. [26].

In this work, the effects of heat treatments on the microstructure, phase formation/dissolution, and hardness on both deposited material and substrate have been studied. For that purpose, an Inconel 718 dove tail geometry has been deposited on a same material

forged sheet substrate, as a representative complex geometry for the application of feature addition by DED. Both additive and forged material defects and microstructure properties, as-deposited and heat-treated conditions, after undergoing different heat treatments have been studied and presented in this paper. In addition, evolution of the mechanical properties through hardness values in different region of the structure for each sample also was also evaluated.

2. Materials and Methods

2.1. Materials

A nickel-based alloy chemically equivalent to Inconel 718 was used as both the filler and the substrate material in the experimental tests. Filler material came in powder form with a granulometry between 45 and 150 µm, from Flame Spray Technologies (FST, Duiven, The Netherland). Substrate material was a forged sheet piece (70 mm × 40 mm × 13.7 mm) in a solution annealed state from ATI (ATI, Pittsburgh, PA, USA). Table 1 presents the chemical composition of the powder and the substrate materials. Alloy 718 presents excellent oxidation and corrosion-resistant properties at high temperatures (up to 980 °C), hence its widespread use in the aeronautical sector.

Table 1. Chemical composition of Alloy 718 powder and substrate (wt. %).

	Ni	Cr	Fe	Nb + Ta	Mo	Ti	Al	C	Cu
Powder	53.8	18.9	Bal.	4.8	3.3	0.7	0.2	0.03	0.03
Substrate	52.4	18.1	Bal.	5.2	2.9	1	0.6	0.05	0.02

All tests were performed on an IBARMIA ZVH45/1600 Add+Process hybrid machine (Figure 1). This multiprocess machine (Ibarmia, Azkoitia, Spain) combines DED technology with a 5-axis milling and turning (horizontal and vertical) capability. It is equipped with a Precitec YC52 cladding head (Precitec, Gaggenau, Germany), a Sulzer Metco TWIN-10-C Powder Feeder (Oerlikon Metco, Freienbach, Switzerland), and a Yb-Fiber Rofin FL030 3 kW Laser generator (Coherent Rofin, Santa Clara, CA, USA) with a continuous wavelength of 1.07 µm. The hybrid machine was fitted with a 4-stream coaxial discrete nozzle from Precitec.

Figure 1. IBARMIA ZVH45/1600 Add+Process hybrid machine.

2.2. Dove Tail Geometry Manufacturing

Dove tail geometry was selected as a complex geometry for the feature addition application since it allowed to evaluate the structure obtained and the effect of the heat treatments in a variable thickness geometry.

The dimensions of the target structure were a 50 mm in length wall with a dove tail cross section that starts on the substrate with a width of 7 mm increasing in both edges at 65° wall angle (θ) until reach a total height of 15.6 mm (Figure 2).

Figure 2. Dove tail structure, cross section.

Strategy for manufacturing a demanding geometry with a multilayer structure of variable thickness as a dove tail geometry, is based on the strategy developed in previous works for multilayered structures of variable thickness [27–29], where complex geometries were deposited tilting the nozzle on a horizontal substrate.

Starting each layer at the same side and employing a zigzag strategy with the opposite direction to the previous layer as the cladding path studied by Kono et al. [30], the first clad is tilted according to the angle of the starting side. The second clad is deposited vertically as a transition clad before tilting the laser head according to the other side angle maintaining this angle until the last clad of the layer (Figure 3). In order to obtain the tool path according to these requirements, the trajectory was programed employing Python software.

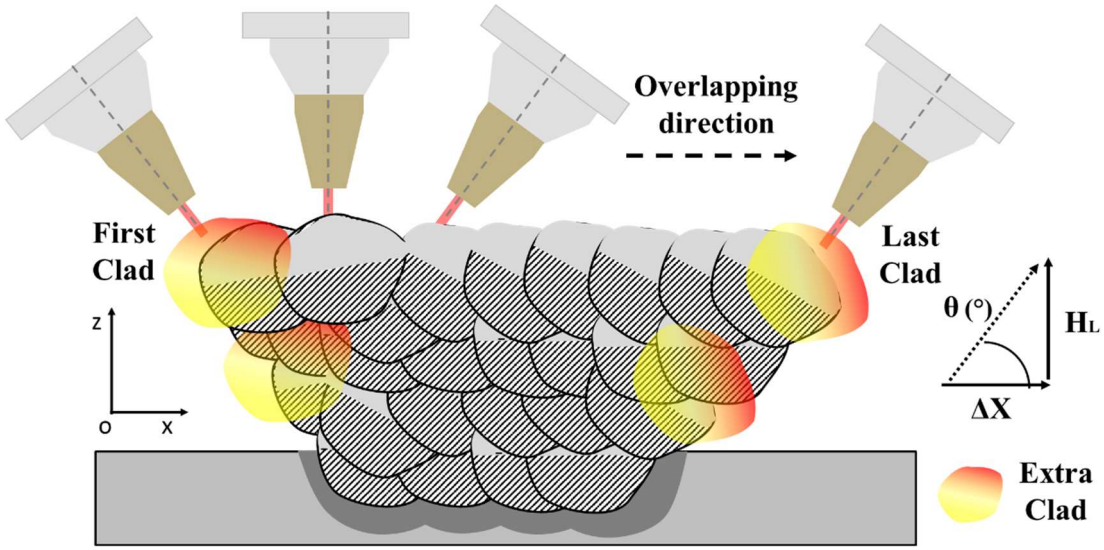

Figure 3. Scheme of the deposition strategy. Dove tail cross section.

Optimum working conditions obtained from previous works [27] were selected for alloy 718 deposition through the 4-stream nozzle. All other processing variables were held constant considering previous experience. The working distance was 14.5 mm. Argon was

employed as both carrier and protective gas, at flow rates of 4.5 and 18 L·min^{-1}, respectively, using a laser spot size of 2.6 mm. The process main parameters are summarized in Table 2.

Table 2. Main deposition parameters.

P (W)	v (mm·min^{-1})	$\dot{m}_p$ (g·min^{-1})	d_o (%)	H_L (mm)	ΔX (mm)	θ (°)
2500	500	18	40–60	1.2	0.56	65

2.3. Heat Treatments and Microstructure Evaluation

DED as-fabricated material presents typically columnar dendritic structure with large grain sizes, which tends to reduce mechanical behavior, toughness and surface quality of manufactured parts. In order to improve the directional microstructure and anisotropy of the material, how the heat treatment methods industrially applied for cast or wrought Inconel 718 affect the deposited material microstructure has been investigated in the literature. The most commonly employed treatments in the literature are:

1. Homogenization treatment: to homogenize the segregated elements, dissolve detrimental phases such as Laves phase and full recrystallization of cast or wrought structure.
2. Solution treatment: the solution cycle is usually the same as homogenization, but it serves a different purpose. This treatment is intended to dissolve second phases in the γ matrix to produce maximum corrosion resistance or to prepare an alloy for subsequent aging.
3. Aging (precipitation process): this treatment causes the precipitation of strengthening phases (γ' and γ'') from the supersaturated matrix by solution treating, improving mechanical properties.

Due to the lack of published scientific works about heat treatments for powder-fed DED materials, heat treatments studied in different works employing other additive processes have been consulted and summarized in Table 3.

Table 3. Heat treatments applied for Inconel 718 in different articles: (AC) air cooling, (WC) water cooling, (FC) furnace cooling.

Article	Homogenization	Solution	Aging (2 Steps)
Qi et al. [26]	1093 °C/2 h/AC	954–982 °C/1 h/AC	718 °C/8 h/FC 621 °C/10 h/AC
Zhong et al. [31]	1093 °C/2 h/AC	954–982 °C/1 h/AC	718 °C/8 h/FC 621 °C/10 h/AC
Kirka et al. [32]	-	1066 °C/1 h/AC	760 °C/10 h/FC 650 °C/10 h/AC
Zaharia et al. [33]	1080 °C/1.5 h/AC	980 °C/1 h/AC	720 °C/8 h/FC 620 °C/8 h/AC
Zhang et al. [34]	1080 °C/1.5 h/AC	980 °C/1 h/AC	720 °C/8 h/FC 620 °C/8 h/AC
Chlebus et al. [35]	-	980 °C/1 h/WC 1040 °C/1 h/WC 1100 °C/1 h/WC	720 °C/8 h/FC 620 °C/10 h/AC

Qi et al. [26] and Zhong et al. [31] used the same heat treatment conditions in a vertically deposited powder-fed DED part at a laser power of 550 W and 2950 W, respectively. The only difference was the Hot Isostatic Pressure (HIP) treatment employed by Zhong et al. prior to the heat treatment to reduce the resulting porosity in the deposited material. In both studies, homogenization resulted in an equiaxed microstructure and mechanical properties in line with Aerospace Material Specifications (AMS) for cast and wrought Inconel 718.

Kirka et al. [32] deposited a square-shaped structure by electron beam melting (EBM) method at 60 kV with a preheating temperature of 975 °C during the process, then it was followed by HIP treatment and solution treatment at 1066 °C for 1 h, in order to preserve the columnar structure with elastic and fracture strength in accordance with ASTM F-3055. According to the work of Abarasan et al. [36], the temperature and processing time of the solution heat treatment employed in this work should be enough to obtain an equiaxed structure. However, the effect obtained in the deposited material by Kirka et al. disagrees with the effect obtained in Inconel 718 sheets by Abarasan et al.

Finally, Zaharia et al. [33], Zhang et al. [34], and Chlebus et al. [35] heat treated structures deposited by Powder Bed Fusion (PBF) process at 200 W, 400 W, and 100 W, respectively. The posthomogenization microstructure in the work of Zaharia et al. and Zhang et al. showed globally uneven recrystallized grains and only partial recrystallization. In the case of Chlebus et al., the recrystallization was obtained without homogenization step increasing solution treatment temperature at 1100 °C. In works by both Zhang et al. and Chlebus et al., the mechanical properties agree with the results of Qi et al. and Zhong et al. In summary, the heat treatments applied to Inconel 718 in different articles that comply with the Aerospace Materials Specification (AMS) are shown in Table 3.

Heat treatment for a full recrystallization depends on both the temperature reached and the holding time. As obtained by Miao et al. [37], longer holding time increases the dissolution of detrimental phases and reduce the segregation in cast Inconel 718. This agrees with the work of Fayed et al. [38], heat treating at 1080 °C a PBF structure. Fayed et al. concluded that a one-hour homogenization treatment was not enough to change the as-fabricated texture and grain structure, obtaining complete recrystallization and more dissolution of detrimental phases after 4 h. However, after 4 h homogenization treatment, more carbide particles were formed and after 7 h, the structure resulted in grain growth and carbides coarsening that could result in lower fatigue resistance [39]. These results after 4 h homogenization agree with the results of Mostafa et al. [40] after 4 h HIP treatment of a PBF structure.

After evaluating previous works, and in order to evaluate the different heat treatment effects on the microstructure of a dove tail geometry, cross sections of 4 samples with the following heat treatments were analyzed:

1. As-deposited;
2. Homogenization (H): 1100 °C/2 h/AC;
3. Direct aging (A): 718 °C/10 h/FC + 621 °C/10 h/AC;
4. Solution treatment and aging (STA): 1100 °C/2 h/AC + 718 °C/10 h/FC + 621 °C/10 h/AC.

Samples were heat-treated, sectioned, polished, and etched with Kallings etchant. Microstructures at different heat treatment conditions were examined by optical microscopy and scanning electron microscopy (SEM) using JEOL JSM 5910 LV (JEOL Ltd., Akishima, Japan) and EDX Oxford INCA X-act spectroscope (Oxford Instruments, Abingdon-on-Thames, UK).

3. Results and Discussion

3.1. Microstructure

Cross section of the samples were cut, polished, and etched for metallographic analysis (Figure 4).

A columnar dendritic structure was obtained as deposited. However, depending on the zone and the height over the substrate, it presented different characteristics. Grain size enlarged with the height due to the increasing of the temperature during the process and the decreasing of the cooling rate. In the edge of the cross sections (where highest temperature and lowest cooling rates are reached), long columnar grains of several millimeters, non-existent in the rest of the cross section, were observed. Additionally, some isolated pores of less than 40 μm were detected in the structure.

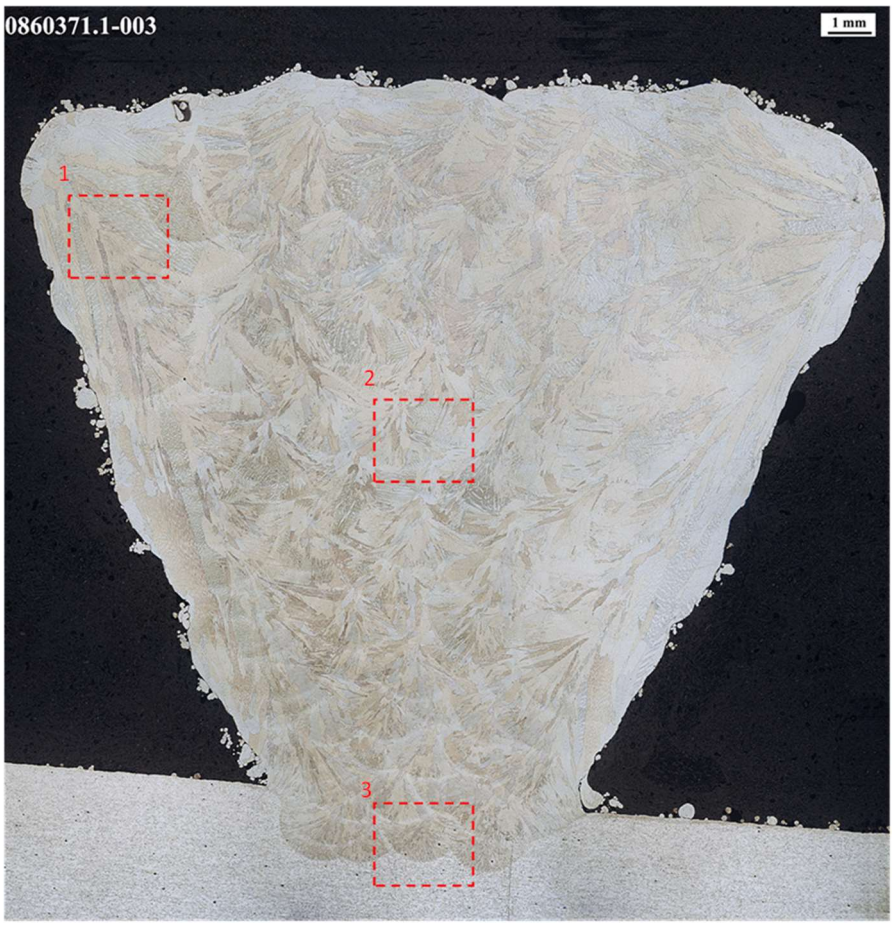

Figure 4. Control structure. As deposited. Zone 1: edge of the cross-section; Zone 2: core of the cross-section; Zone 3: first deposited layer and dilution zone with the substrate.

The structure obtained in the direct aged sample remains similar to the as-deposited structure. On the contrary, both the homogenized and STA samples presented non-dendritic columnar structure due to the dissolution of secondary phases in the nickel matrix. Melt pool boundaries were clearly visible in the as-deposited and direct aged samples. This is attributed to the lower dendritic structure in that zone caused by the rapid cooling. After the dissolution of detrimental phases, these melt pool boundaries disappeared in both the homogenized and STA samples.

Evolution of the structure, regarding the as-deposited state, in different zones of the cross section was analyzed to define the effects of the applied heat treatments. This evolution can be defined analyzing three zones (Figure 4):

1. Edge of the cross-section geometry;
2. Core of the cross-section;
3. First deposited layer and dilution zone with the substrate.

The long columnar grain size on the edges of the cross-section remains constant in all samples regardless of the heat treatment (Figure 5). This occurs because the grain size affects the critical temperature for the recrystallization, resulting in a decrease in the nucleation rate and hence an increase in the recrystallization temperature. In the samples with dendritic structure (as-deposited and direct-aged), the dendritic growth orientation in the deposition starting side was sharply different due to the different tilting angle of the laser head in the first three deposited clads (Figure 5c).

Furthermore, grains obtained in the core of the cross section presented a slight effect after homogenization and solution treatments (Figure 6). As in the edges of the cross section, this results in a remain of the columnar structure.

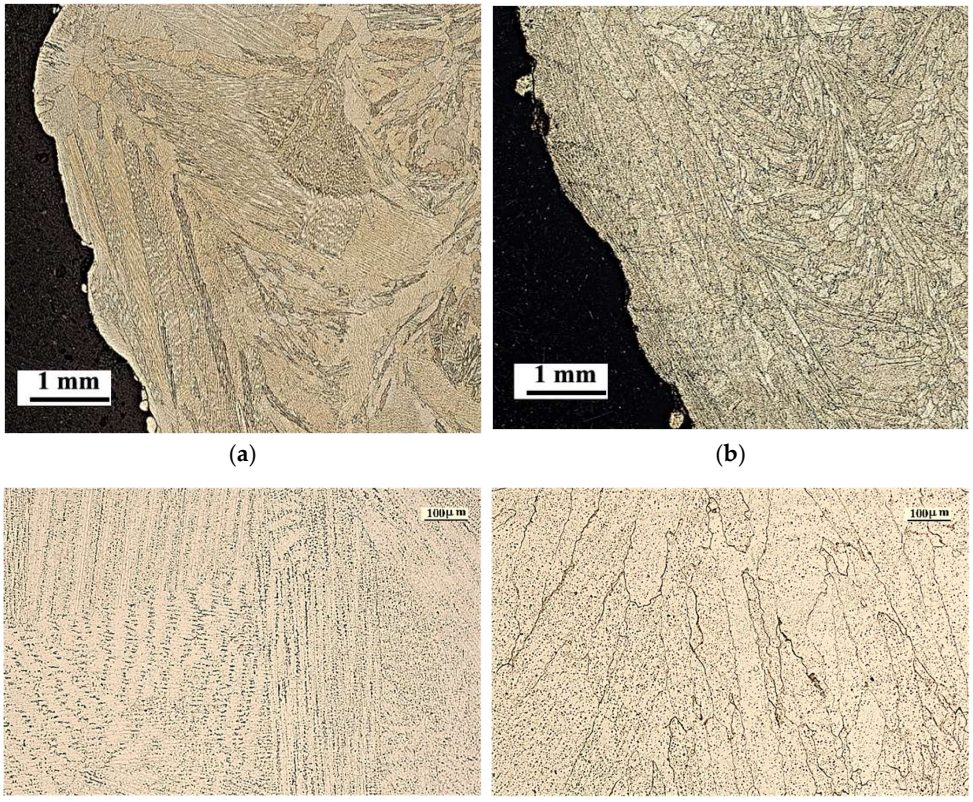

(**a**) (**b**)

(**c**) (**d**)

Figure 5. Cross-sections structure on the upper zone: (**a**,**c**) as-deposited; (**b**,**d**) solubilization and aging (STA).

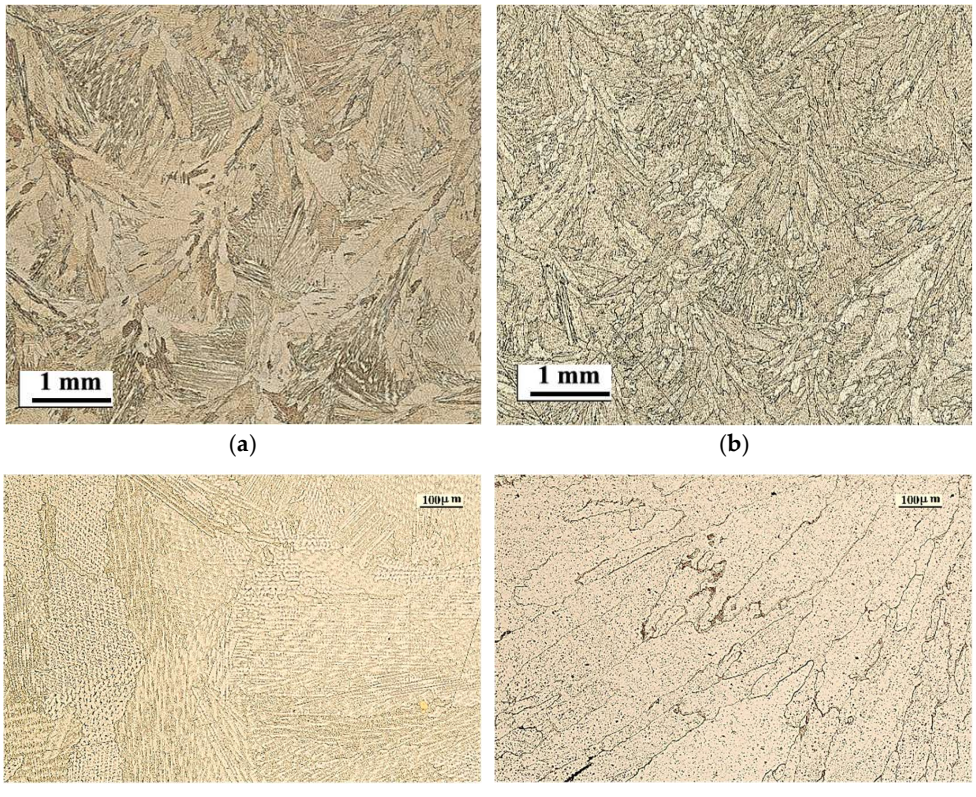

(**a**) (**b**)

(**c**) (**d**)

Figure 6. Cross-sections structure on the core: (**a**,**c**) as-deposited; (**b**,**d**) solubilization and aging (STA).

Finally, the first deposited layer and dilution zone with the substrate presented some uneven overall recrystallized grains after the homogenization and solution treatment (Figure 7), including some isolated annealing twins in the dilution zone (Figure 7d). Grain size decreasing results in more boundaries, and therefore, this results in a recrystallization of the smallest grains of the structure in this zone because grain boundaries are good sites for nuclei forming.

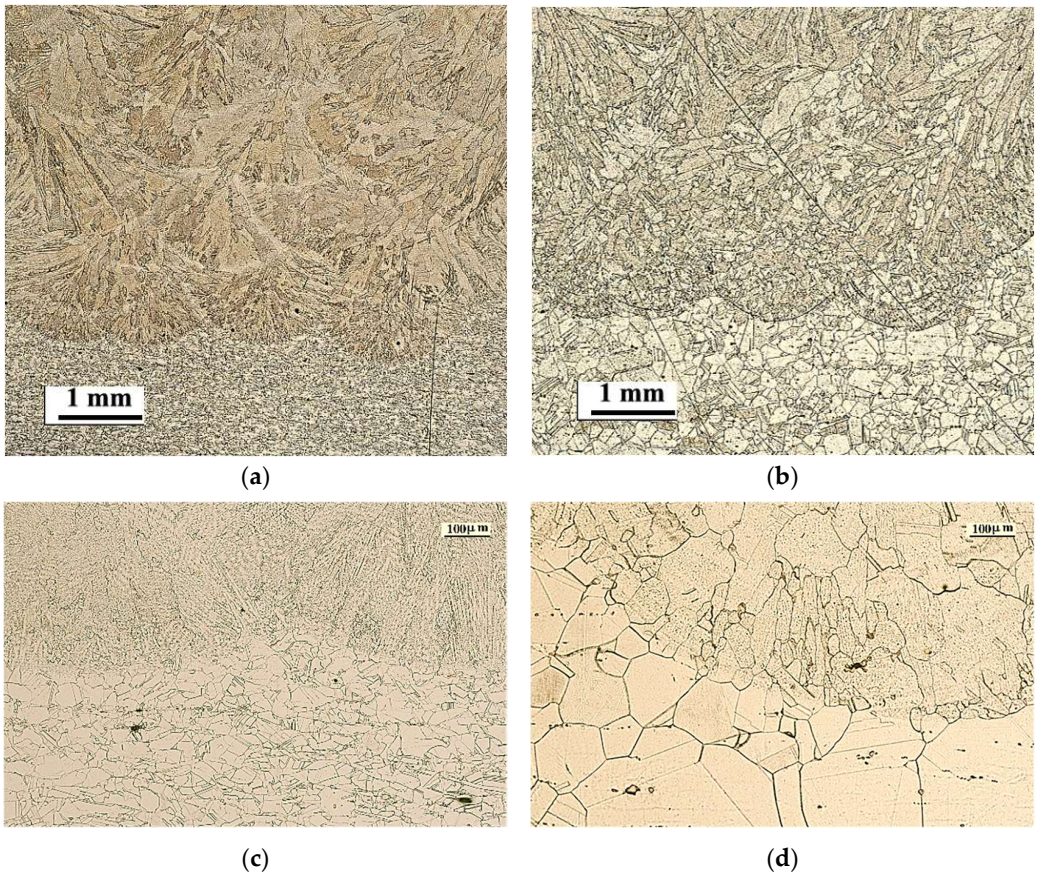

Figure 7. Cross-sections structure on the dilution zone: (**a**,**c**) as-deposited; (**b**,**d**) solubilization and aging (STA).

The substrate presented the expected heat treatment effects, increasing sharply the grain size after the recrystallization after both homogenization and solution treatments due to even and small initial grain size. Thus, the results obtained after both homogenization and STA in different zones of the cross section agree with the results of different works depending on the initial grain size.

Due to the large grain size obtained under high laser power conditions, common heat treatments do not produce recrystallization of the deposited material, which excludes an uneven overall crystallization in the dilution zone and the first deposited layer due to the lower initial grain size obtained in this zone during deposition. This fact, combined with the sharply increase in the grain size in the substrate, demands a different heat-treating process in order to obtain an appropriate structure, finer grains, and better mechanical properties, when adding features by powder-fed DED. In AM materials, grain refinement is possible by adding nucleant alloys to the material (as discussed Zhang et al. [41]), by severe plastic deformation, or combining both solutions. Increasing deformation, both the recrystallization temperature and the grain size are decreased. Several works studied this way of improving the structure of deposited materials, as did Sizova et al. [42] and Bambach et al. [43], combining the additive process with a latter forging process, and Xie et al. [44], Santos et al. [45], and Moeini et al. [46] with a latter Stir Friction process.

3.2. Hardness

Hardness was measured at different points of the cross sections, both in the deposited material and substrate, resulting in a highest hardness in the core of the deposited cross-section. The mean results are shown in Table 4.

Table 4. HV hardness. Mean value and variability.

HV	As-Deposited	Direct Aging	Homogenization	STA
Deposited	255 (±48)	397 (±26)	183 (±18)	415 (±21)
Substrate	248 (±31)	441 (±6)	158 (±6)	312 (±23)

In the as-deposited sample, hardness obtained both in deposited material and substrate were very similar. In the direct-aged sample, a notorious increase in the hardness on both deposited material and substrate was obtained and corresponded with the precipitation of strengthening phases γ' and γ'' (Figure 8). This is a normal effect of the aging heat treatment in the substrate since material was supplied in the solution annealed condition, but not in the deposited material, despite no previous solution treatment having been applied.

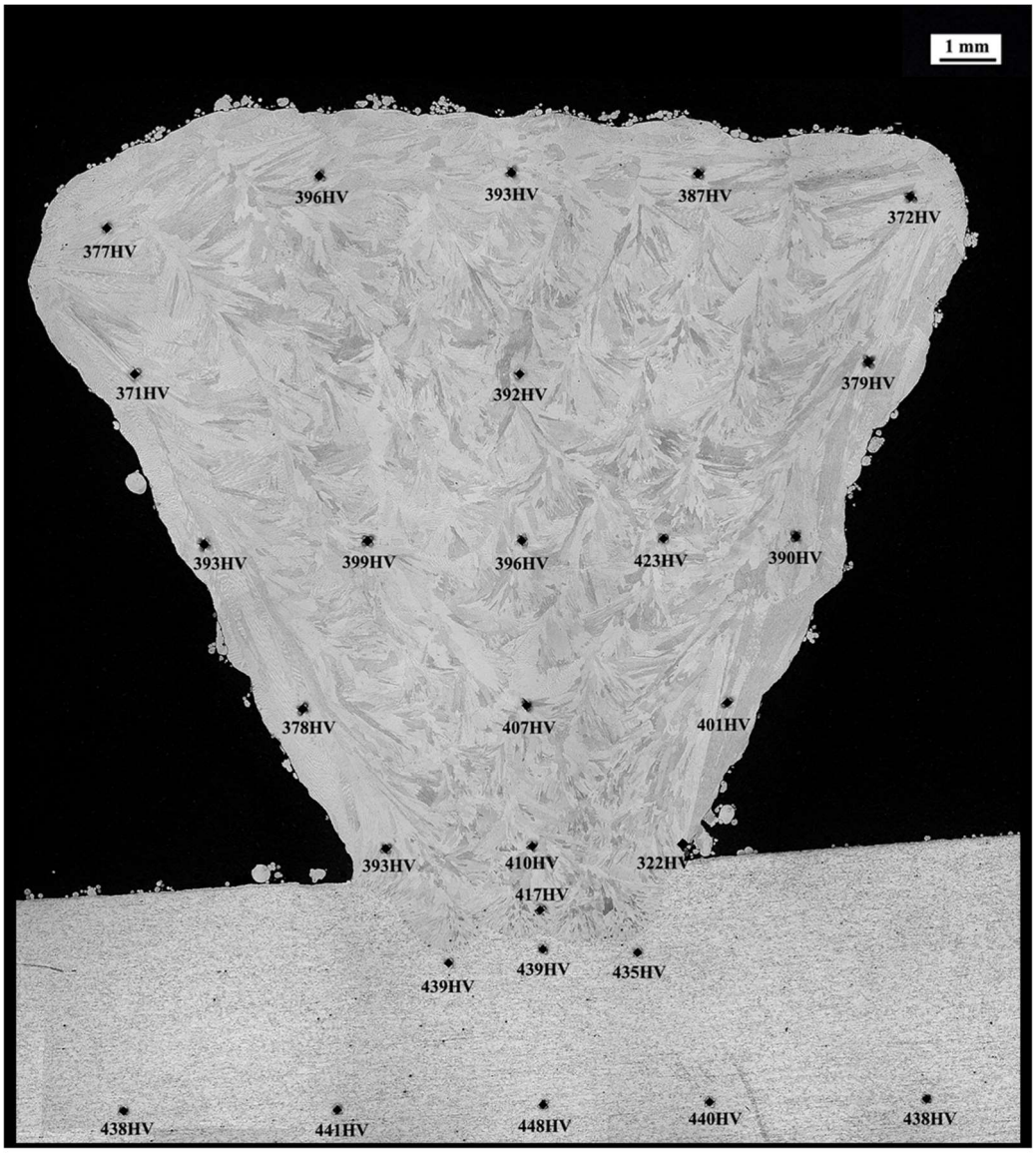

Figure 8. Hardness profile of the direct aged sample.

As expected, hardness decreased after homogenization treatment, especially in the substrate, due to the sharp increase in the grain size. Since the homogenization and solution treatment were performed under the same conditions, this fact explains the decreasing in the hardness obtained in the substrate after the STA treatment (Figure 9). On the contrary, hardness obtained in the deposited material after the STA treatment increased comparing to the direct-aged sample due to the dissolution of second phases in the γ matrix during the solution treatment.

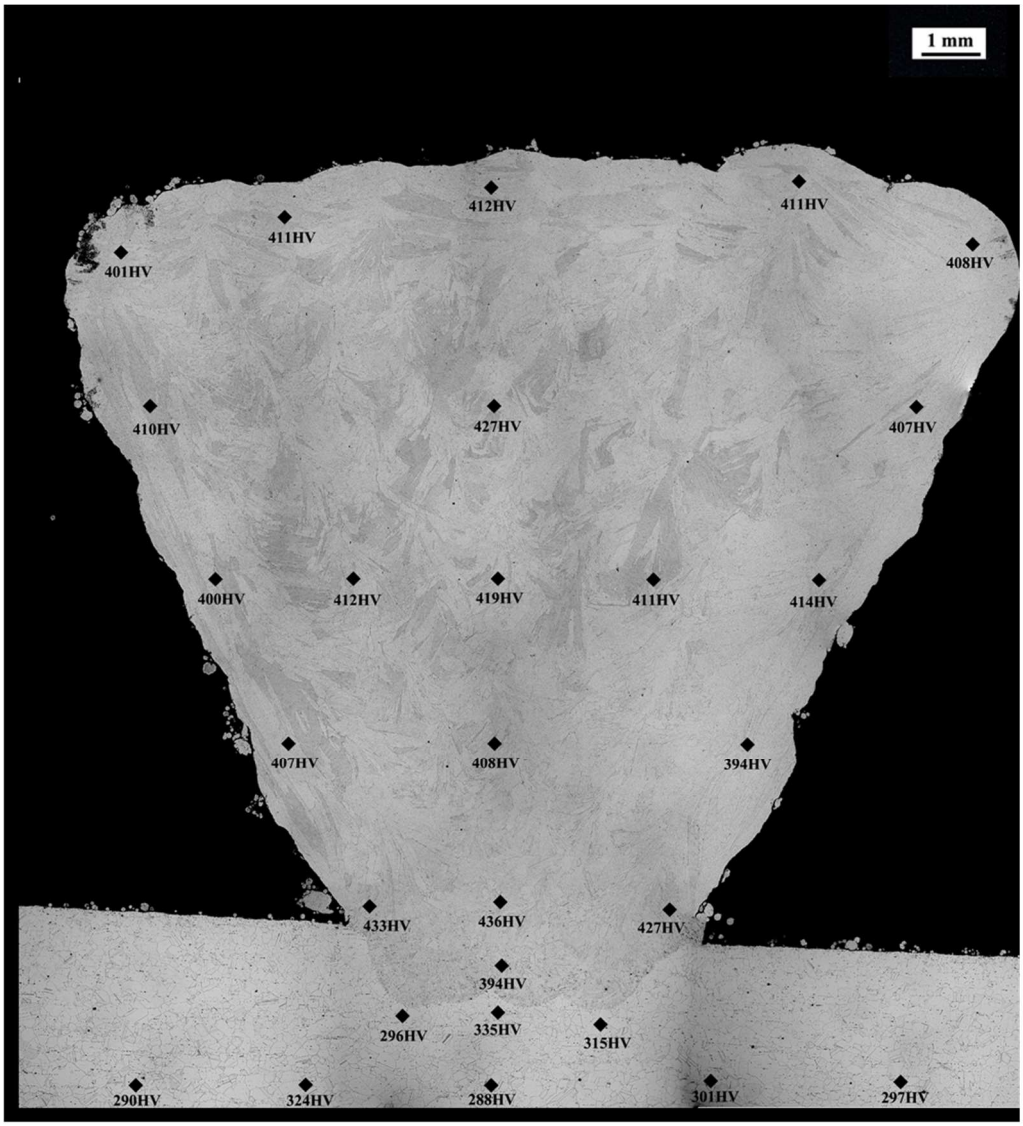

Figure 9. Hardness profile of the STA sample.

The results in Table 5 compare the hardness obtained in the top, middle, first layer, and substrate of all samples.

3.3. SEM Analysis

In the as-deposited and direct-aged samples, a large number of white irregular shape phases and some grey and black blocky particles were precipitated in the interdendritic boundaries (Figure 10a,d). White particles were identified as Laves phase and some minor Nb-rich MC phase (Figure 10b,c). On the other hand, there were several grey and black precipitates uniformly dispersed identified as TiN phase and aluminum oxides, respectively (Figure 10d,f).

Table 5. HV hardness in top, middle, first layer, and substrate of all samples.

Zone	Sample	Hardness (HV)				
Top	As-deposited	236	244	228	215	216
	Aged	377	396	393	387	372
	Homogenized	170	179	181	176	171
	STA	401	411	412	411	408
Middle	As-deposited	251	267	262	247	215
	Aged	393	399	396	423	390
	Homogenized	173	186	193	192	176
	STA	400	412	419	411	414
First layer	As-deposited		303	289	276	
	Aged		393	410	322	
	Homogenized		190	200	198	
	STA		433	436	427	
Substrate	As-deposited	220	227	217	223	223
	Aged	438	441	448	440	438
	Homogenized	154	152	163	159	159
	STA	290	324	288	301	297

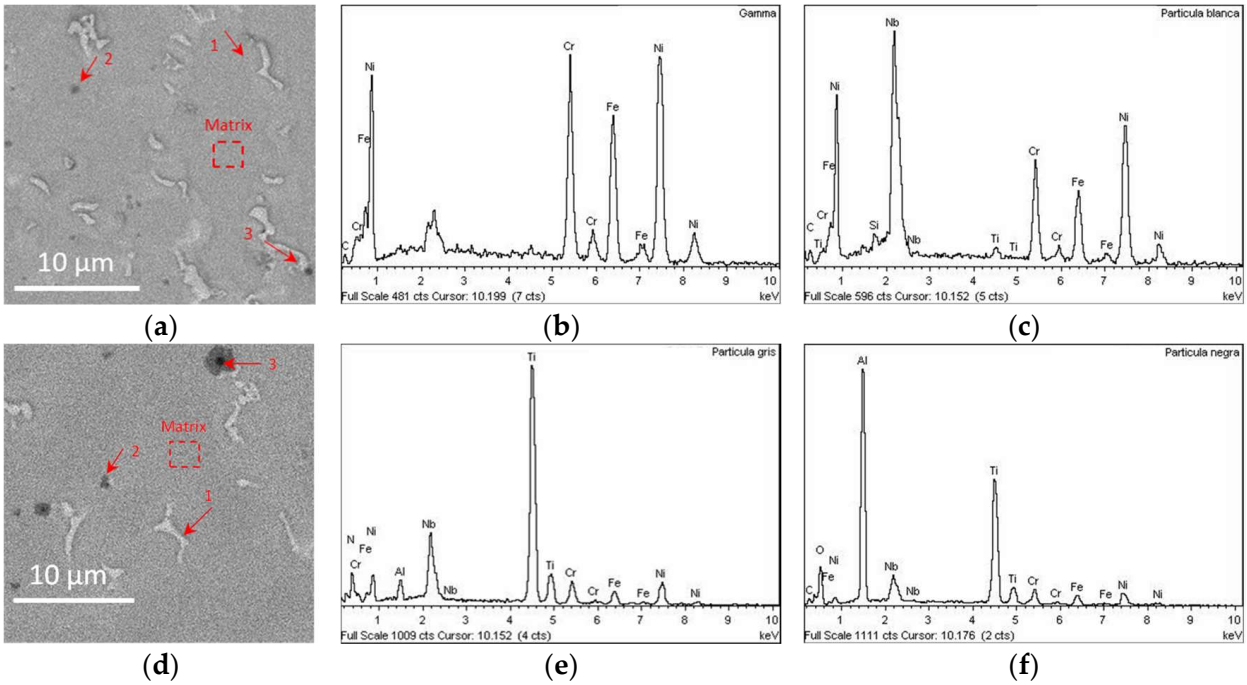

Figure 10. SEM analysis: (**a**) as-deposited sample; (**d**) direct-aged sample; (**b**) matrix EDS; (**c**) 1-white particle EDS (Laves phase); (**e**) 2-Grey particle EDS; (**f**) 3-Black particle EDS.

Since oxide inclusions normally tend to act as nucleation sites for other precipitates, there were different size, morphology, and distributed titanium nitrides and some minor titanium carbonitrides around the aluminum oxide particles in all samples.

In the homogenized and STA samples, the high temperature of homogenization and solution (at 1100 °C) dissolved most Laves phase (Figure 11a,d). White Nb-rich MC, grey TiN, black oxides, and carbonitrides are relatively stable phases and were found in both samples (Figure 11).

In the as-deposited and direct-aged substrate samples (Figure 12a,d), there were only some disperse grey TiN, black Al-rich oxides and larger-size white Nb-rich carbides (Figure 12). In the case of the Nb-rich carbides, the size obtained in the substrate was larger than 10 µm, meanwhile, in the deposited material were obtained few microns size particles.

However, the substrate presented small precipitates in the grain boundaries in contrast to the additively deposited structure.

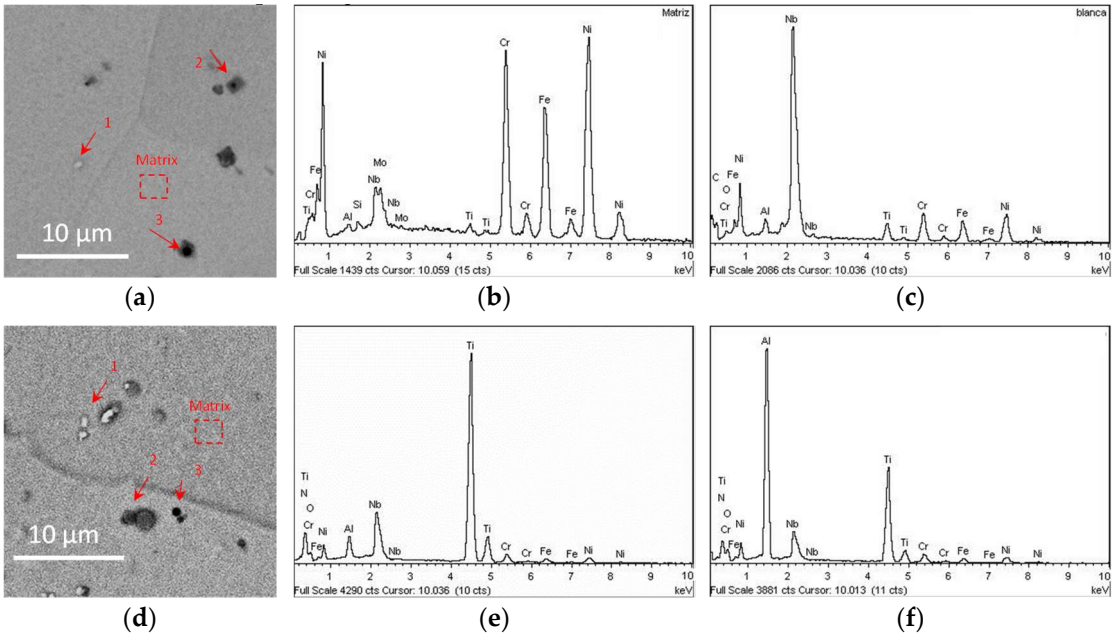

Figure 11. SEM analysis: (**a**) Homogenized sample; (**d**) STA sample; (**b**) matrix EDS; (**c**) 1-white particle EDS; (**e**) 2-Grey particle EDS; (**f**) 3-Black particle EDS.

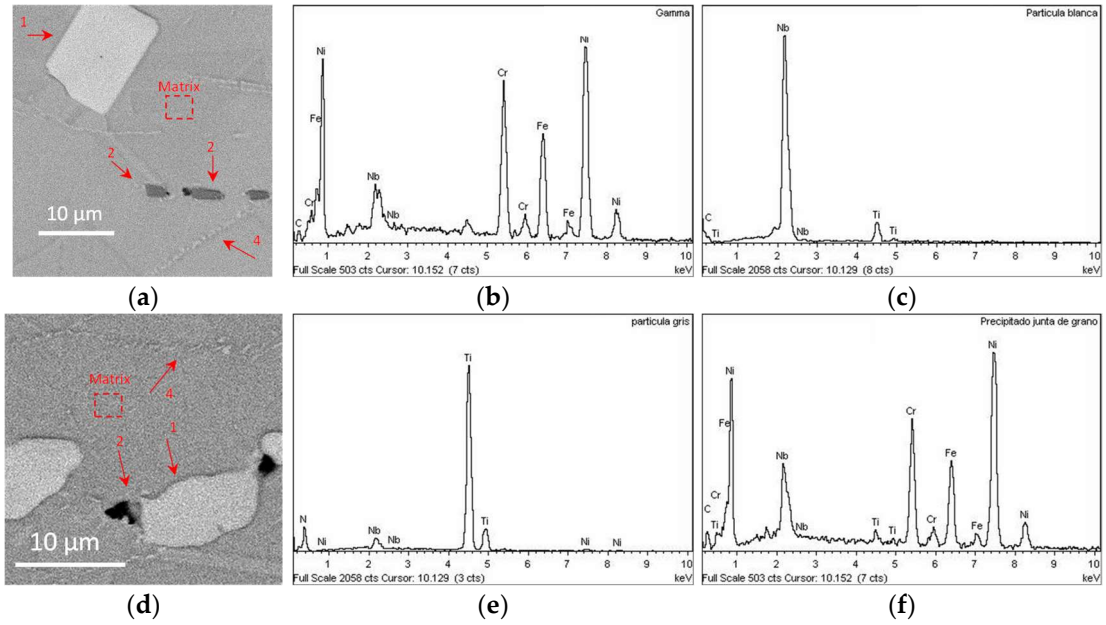

Figure 12. Substrate SEM analysis: (**a**) as-deposited sample; (**d**) direct-aged sample; (**b**) matrix EDS; (**c**) 1-white particle EDS; (**e**) 2-Grey particle EDS; (**f**) 4-grain boundaries EDS.

These precipitates presented greater Nb content than the matrix as the δ phase or Nb-rich carbides (Figure 12f), but identification of these small precipitates is complex by SEM since the EDS overlaps with the matrix. In further studies, it would be necessary to employ X-ray Powder Diffraction (XRD) or Transmission electron microscopy (TEM) for the identification of these precipitates.

Finally, in the homogenized and STA substrate samples (Figure 13a,d), the high temperature of homogenization and solution (at 1100 °C) dissolved the precipitates observed in the grain boundaries of the as-deposited and direct-aged substrate samples.

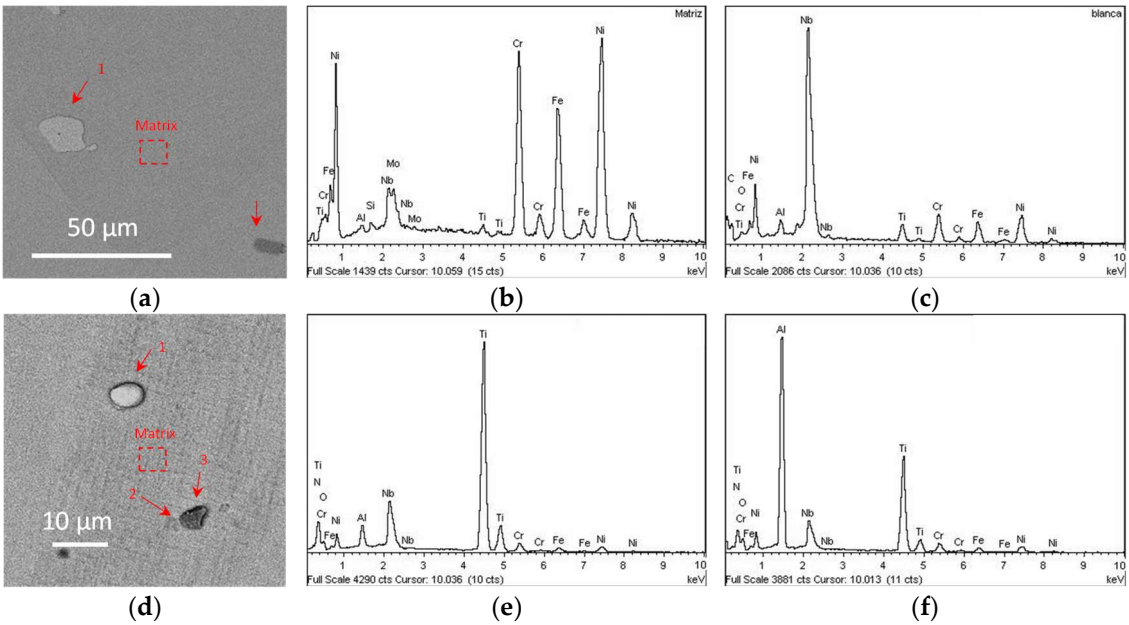

Figure 13. Substrate SEM analysis: (**a**) Homogenized sample; (**d**) STA sample; (**b**) matrix EDS; (**c**) white particle EDS; (**e**) Grey particle EDS; (**f**) Black particle EDS.

The material presented a grearer amount of TiN and oxides in the additively deposited structure than in the substrate. This phenomenon must be further studied, as did Chen et al. [47] and Yu et al. [48], to measure the effects produced by TiN and oxides content both on mechanical properties and on the live span of the component.

Figure 14 presents the composition of both the deposited and substrate matrix in all samples, and substrate grain boundaries precipitates in the as-deposited and aged samples. As the substrate matrix presented the same element content in all samples, it has been represented by only one value. This analysis is only a semi-quantitative presentation without further standardization.

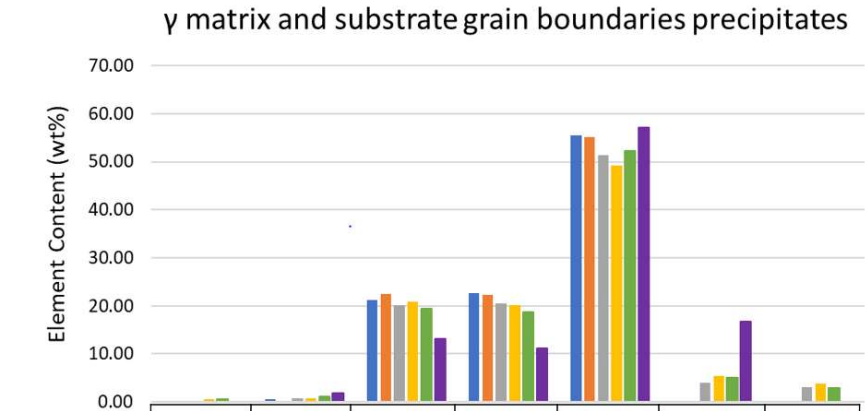

	Al	Ti	Cr	Fe	Ni	Nb	Mo
As deposited	0.00	0.54	21.24	22.69	55.53	0.00	0.00
Aged	0.00	0.00	22.47	22.31	55.21	0.00	0.00
Homogenized	0.26	0.71	20.22	20.53	51.08	4.03	3.17
STA	0.53	0.75	20.81	20.13	48.68	5.37	3.72
Substrate	0.53	1.15	19.36	18.70	52.31	5.00	2.95
Precipitates	0.00	1.80	13.13	11.19	57.21	16.68	0.00

Figure 14. Comparison of γ matrix in the different samples and the grain boundaries precipitates detected in the substrate of as-deposited and aged samples.

As Figure 14 shows, the matrix of the as-deposited and aged material presented lack of Nb and Mo content caused by the formation of the Laves phase due to the segregation of these elements by the slow cooling and long solidification time of the DED process (Figure 15). On the contrary, the temperatures reached in the homogenization and STA treatments dissolved Laves phase and, consequently, dissolved Nb and Mo elements in the matrix.

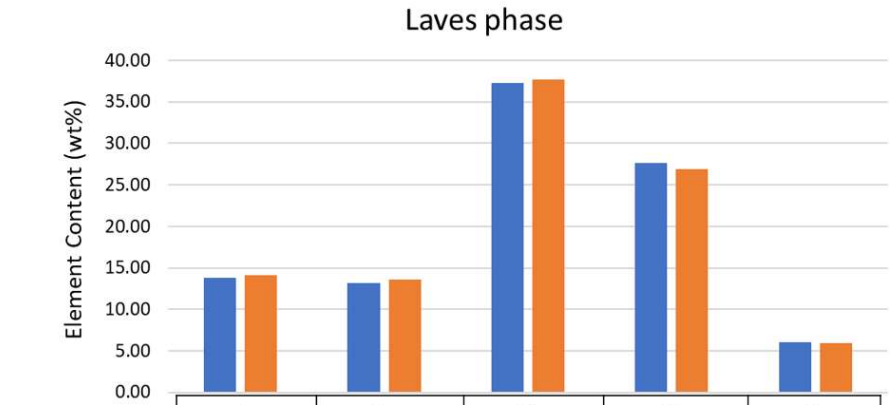

	Cr	Fe	Ni	Nb	Mo
As deposited	13.84	13.14	37.32	27.61	6.05
Aged	14.16	13.55	37.65	26.94	5.89

Figure 15. Comparison of Laves phase in the as-deposited and aged samples.

The segregation of Nb and Mo elements in the Laves phase in the aged sample (Figure 15) does not correspond with the typical precipitation of strengthening phases γ' and γ'' in the matrix and suggests some local precipitation of these strengthening phases out of the matrix, possibly around Laves phases due to its Nb content, but it was not possible to corroborate it by SEM due to the small size of these phase. As commented, in further studies, it would be necessary to employ XRD or TEM for the identification of the strengthening mechanisms of the aged deposited material.

Finally, despite EDS overlapping with the matrix, the higher content of niobium and nickel in the grain boundaries of the substrate in the as-deposited and aged samples, and the dissolution of the observed precipitates in the grain boundaries after homogenization and STA treatments (Figure 14), suggest the presence of δ phase.

4. Conclusions

Due to the large grain size obtained under high laser power conditions, common heat treatments do not produce recrystallization of the deposited material, which excludes an uneven overall crystallization in the dilution zone and the first deposited layer due to the smaller initial grain size obtained in this zone during deposition.

Notorious increase in the hardness on deposited material was obtained in the direct aged sample. This increase could be caused by some local precipitation of strengthening phases out of the matrix, possibly around Laves phases due to its Nb content. In further studies, it would be necessary to employ XRD or TEM for the identification of the strengthening mechanisms of the aged deposited material.

Both additive part and substrate presented Nb-rich carbides, although the size of these particles was much larger in the substrate reaching 10 μm size. However, the additively deposited material presented a larger amount of TiN and oxides in the structure and lower precipitates in the grain boundaries than the substrate. In further studies, it would be necessary to study the effects produced by TiN and oxides content on mechanical properties and on the lifespan of the component.

Author Contributions: Conceptualization, P.R. and H.G.; methodology, P.R., A.P.-C. and H.G.; software, P.R.; validation, P.R. and M.O.; formal analysis, P.R., M.O. and A.P.-C.; investigation, P.R., H.G. and A.P.-C.; resources, A.A., E.M. and H.G.; data curation, P.R., H.G. and A.P.-C.; writing—original draft preparation, P.R., H.G., E.U.; writing—review and editing, P.R., T.B., M.O., A.P.-C., A.A., E.U. and H.G.; visualization, P.R. and T.B.; supervision, A.A., E.M. and H.G.; project administration, A.A., E.M. and H.G.; funding acquisition, A.A., E.M. and H.G. All authors have read and agreed to the published version of the manuscript.

Funding: This research was funded by the vice-counsel of technology, innovation and competitiveness of the Basque Government (Eusko Jaurlaritza) under the ELKARTEK Program, QUALYFAM and EDISON projects, grant number KK-2020/00042 and KK-2022/00070, respectively.

Institutional Review Board Statement: Not applicable.

Informed Consent Statement: Not applicable.

Data Availability Statement: Not applicable.

Conflicts of Interest: The authors declare no conflict of interest. The funders had no role in the design of the study; in the collection, analyses, or interpretation of data; in the writing of the manuscript, or in the decision to publish the results.

Nomenclature

Symbol	Description	Unit
AC	Air cooling	-
AM	Additive Manufacturing	-
AMS	Aerospace Material Specifications	-
ASTM	American Society for Testing and Materials	-
DED	Directed Energy Deposition	-
d_O	Overlap percentage between adjacent clads	%
EBM	Electron Beam Melting	-
EDS	Energy Dispersive Spectrometer	-
FC	Furnace cooling	-
H_L	Layer height	mm
MDR	Mass Deposition Rate	$Kg \cdot h^{-1}$
$\dot{m}_p$	Powder mass flow rate	$g \cdot min^{-1}$
N_C	Number of clads per layer	-
P	Laser power	W
PBF	Powder Bed Fusion	-
SEM	Scanning Electron Microscope	-
v	Feed rate	$mm \cdot min^{-1}$
WC	Water cooling	-
ΔX	Horizontal displacement	mm
θ	Wall angle	$^\circ$

References

1. Chadha, U.; Abrol, A.; Vora, N.P.; Tiwari, A.; Shanker, S.K.; Selvaraj, S.K. Performance evaluation of 3D printing technologies: A review, recent advances, current challenges, and future directions. *Prog Addit. Manuf.* **2022**, *7*, 2363–9520. [CrossRef]
2. Dass, A.; Moridi, A. State of the Art in Directed Energy Deposition: From Additive Manufacturing to Materials Design. *Coatings* **2019**, *9*, 418. [CrossRef]
3. Ramiro, P.; Alberdi, A.; Ortiz, M.; Lamikiz, A.; Ukar, E. Characteristics of Fe-, Ni- and Co-based powder coatings fabricated by laser metal deposition without preheating the base material. *Procedia CIRP* **2018**, *68*, 381–386. [CrossRef]
4. Ramiro, P.; Ortiz, M.; Alberdi, A.; Lamikiz, A. Characteristics of Fe-based powder coatings fabricated by laser metal deposition with annular and four stream nozzles. *Procedia CIRP* **2018**, *74*, 201–205. [CrossRef]
5. Ramiro, P.; Ortiz, M.; Alberdi, A.; Lamikiz, A. Optimization of the efficiency of the laser metal deposition process applied to high hardness coatings by the analysis of different types of coaxial nozzles. *DYNA* **2018**, *93*, 613–619. [CrossRef]
6. Zhong, C.; Biermann, T.; Gasser, A.; Poprawe, R. Experimental study of effects of main process parameters on porosity, track geometry, deposition rate, and powder efficiency for high deposition rate laser metal deposition. *J. Laser Appl.* **2015**, *27*, 042003. [CrossRef]

7. Zhong, C.; Pirch, N.; Gasser, A.; Poprawe, R.; Schleifenbaum, J.H. The Influence of the Powder Stream on High-Deposition-Rate Laser Metal Deposition with Inconel 718. *Metals* **2017**, *7*, 443. [CrossRef]
8. Li, Z.; Chen, J.; Sui, S.; Zhong, C.; Lu, X.; Lin, X. The microstructure evolution and tensile properties of Inconel 718 fabricated by high-deposition-rate laser directed energy deposition. *Addit. Manuf.* **2020**, *31*, 100941. [CrossRef]
9. Lu, J.Z.; Cao, J.; Lu, H.F.; Zhang, L.Y.; Luo, K.Y. Wear properties and microstructural analyses of Fe-based coatings with various WC contents on H13 die steel by laser cladding. *Surf. Coat. Technol.* **2019**, *369*, 228–237. [CrossRef]
10. Foster, J.; Cullen, C.; Fitzpatrick, S.; Payne, G.; Hall, L.; Marashi, J. Remanufacture of hot forging tools and dies using laser metal deposition with powder and a hard-facing alloy Stellite 21®. *J. Remanufactur.* **2019**, *9*, 189–203. [CrossRef]
11. Ding, Y.; Liu, R.; Yao, J.; Zhang, Q.; Wang, L. Stellite alloy mixture hardfacing via laser cladding for control valve seat sealing surfaces. *Surf. Coat. Technol.* **2017**, *329*, 97–108. [CrossRef]
12. Stoffel, N.J.; Placek, C.; Johnson, K.A.; Baez, H. Agricultural Blades and Machine Parts with Amorphous Metal Laser Cladding. US Patent 9717176B2, 1 August 2017.
13. Nowotny, S.; Brueckner, F.; Thieme, S.; Leyens, C.; Beyer, E. High-performance laser cladding with combined energy sources. *J. Laser Appl.* **2015**, *27*, S17001. [CrossRef]
14. Tuominen, J.; Näkki, J.; Pajukoski, H.; Peltola, T.; Vuoristo, P.; Kuznetsov, M.; Pozdeeva, E.; Zemlyakov, E.V.; Turichin, G.A. Laser cladding with 15 kW fiber laser. In Proceedings of the 13th NOLAMP Conference, Trondheim, Norway, 27–29 June 2011. [CrossRef]
15. Lei, X.; Huajun, C.; Hailong, L.; Zhang, Y. Study on laser cladding remanufacturing process with FeCrNiCu alloy powder for thin-wall impeller blade. *Int. J. Adv. Manuf. Technol.* **2017**, *90*, 1383–1392. [CrossRef]
16. Kaierle, S.; Overmeyer, L.; Alfred, I.; Rottwinkel, B.; Hermsdorf, J.; Wesling, V.; Weidlich, N. Single-crystal turbine blade tip repair by laser cladding and remelting. *CIRP J. Manuf. Sci. Technol.* **2017**, *19*, 196–199. [CrossRef]
17. Merklein, M.; Junker, D.; Schaub, A.; Neubauer, F. Hybrid Additive Manufacturing Technologies–An Analysis Regarding Potentials and Applications. *Phys. Procedia* **2016**, *83*, 549–559. [CrossRef]
18. Meiners, F.; Ihne, J.; Jürgens, P.; Hemes, S.; Mathes, M.; Sizova, I.; Bambach, M.; Hama-Saleh, R.; Weisheit, A. New Hybrid Manufacturing Routes Combining Forging and Additive Manufacturing to Efficiently Produce High Performance Components from Ti-6Al-4V. *Procedia Manuf.* **2020**, *47*, 261–267. [CrossRef]
19. Stadtfeld, H.J. Additive Manufacturing of Gears. Patent No. WO2017095785A1, 29 November 2016.
20. Xu, P.; Lin, C.; Zhou, C.; Yi, X. Wear and corrosion resistance of laser cladding AISI 304 stainless steel/Al_2O_3 composite coatings. *Surf. Coat. Technol.* **2014**, *238*, 9–14. [CrossRef]
21. Carroll, B.E.; Palmer, T.A.; Beese, A.M. Anisotropic tensile behavior of Ti–6Al–4V components fabricated with directed energy deposition additive manufacturing. *Acta Mater.* **2015**, *87*, 309–320. [CrossRef]
22. Roy, T.; Abrahams, R.; Paradowska, A.; Lai, Q.; Mutton, P.; Soodi, M.; Fasihi, P.; Yan, W. Evaluation of the mechanical properties of laser cladded hypereutectoid steel rails. *Wear* **2019**, *432–433*, 202930. [CrossRef]
23. Ostra, T.; Alonso, U.; Veiga, F.; Ortiz, M.; Ramiro, P.; Alberdi, A. Analysis of the Machining Process of Inconel 718 Parts Manufactured by Laser Metal Deposition. *Materials* **2019**, *12*, 2159. [CrossRef]
24. Chew, Y.; Pang, J.; Bi, G.; Song, B. Effects of laser cladding on fatigue performance of AISI 4340 steel in the as-clad and machine treated conditions. *J. Mater. Process. Technol.* **2017**, *243*, 246–257. [CrossRef]
25. Zhao, S.; Yuan, K.; Guo, W.; He, Y.; Xu, Y.; Lin, X. A comparative study of laser metal deposited and forged Ti-6Al-4V alloy: Uniaxial mechanical response and vibration fatigue properties. *Int. J. Fatigue* **2020**, *136*, 105629. [CrossRef]
26. Qi, H.; Azer, M.; Ritter, A. Studies of Standard Heat Treatment Effects on Microstructure and Mechanical Properties of Laser Net Shape Manufactured INCONEL 718. *Metall. Mat. Trans. A* **2009**, *40*, 2410–2422. [CrossRef]
27. Ramiro, P.; Ortiz, M.; Alberdi, A.; Lamikiz, A. Strategy Development for the Manufacturing of Multilayered Structures of Variable Thickness of Ni-Based Alloy 718 by Powder-Fed Directed Energy Deposition. *Metals* **2020**, *10*, 1280. [CrossRef]
28. Ramiro-Castro, P.; Ortiz, M.; Alberdi, A.; Lamikiz, A. Effects of Gravity and Non-Perpendicularity during Powder-Fed Directed Energy Deposition of Ni-Based Alloy 718 through Two Types of Coaxial Nozzle. *Metals* **2020**, *10*, 560. [CrossRef]
29. Ramiro, P.; Ortiz, M.; Alberdi, A.; Lamikiz, A. Geometrical Model and Strategy in Single and Multilayer Structures Deposited by Powder-fed Directed Energy Deposition. *Procedia CIRP* **2020**, *94*, 352–356. [CrossRef]
30. Kono, D.; Maruhashi, A.; Yamaji, I.; Oda, Y.; Mori, M. Effects of cladding path on workpiece geometry and impact toughness in Directed Energy Deposition of 316L stainless steel. *CIRP Annals* **2018**, *67*, 233–236. [CrossRef]
31. Zhong, C.; Gasser, A.; Kittel, J.; Wissenbach, K.; Poprawe, R. Improvement of material performance of Inconel 718 formed by high deposition-rate laser metal deposition. *Mater. Des.* **2016**, *98*, 128–134. [CrossRef]
32. Kirka, M.M.; Medina, F.; Dehoff, R.; Okello, A. Mechanical behavior of post-processed Inconel 718 manufactured through the electron beam melting process. *Mater. Sci. Eng. A* **2017**, *680*, 338–346. [CrossRef]
33. Zaharia, S.M.; Chicoș, L.A.; Lancea, C.; Pop, M.A. Effects of Homogenization Heat Treatment on Mechanical Properties of Inconel 718 Sandwich Structures Manufactured by Selective Laser Melting. *Metals* **2020**, *10*, 645. [CrossRef]
34. Zhang, D.; Niu, W.; Cao, X.; Liu, Z. Effect of standard heat treatment on the microstructure and mechanical properties of selective laser melting manufactured Inconel 718 superalloy. *Mater. Sci. Eng. A* **2015**, *644*, 32–40. [CrossRef]
35. Chlebus, E.; Gruber, K.; Kuźnicka, B.; Kurzac, J.; Kurzynowski, T. Effect of heat treatment on the microstructure and mechanical properties of Inconel 718 processed by selective laser melting. *Mater. Sci. Eng. A* **2015**, *639*, 647–655. [CrossRef]

36. Anbarasan, N.; Gupta, B.K.; Prakash, S.; Muthukumar, P.; Oyyaravelu, R.; Kumar, R.; Jerome, S. Effect of Heat Treatment on the Microstructure and Mechanical Properties of Inconel 718. *Mater. Today Proc.* **2018**, *5*, 7716–7724. [CrossRef]
37. Miao, Z.; Shan, A.; Wu, Y.; Lu, J.; Xu, W.; Song, H. Quantitative analysis of homogenization treatment of INCONEL718 superalloy. *Trans. Nonferrous Met. Soc.* **2011**, *21*, 1009–1017. [CrossRef]
38. Fayed, E.M.; Shahriari, D.; Saadati, M.; Brailovski, V.; Jahazi, M.; Medraj, M. Influence of Homogenization and Solution Treatments Time on the Microstructure and Hardness of Inconel 718 Fabricated by Laser Powder Bed Fusion Process. *Materials* **2020**, *13*, 2574. [CrossRef]
39. Donachie, M.J.; Donachie, S.J. *Superalloys: A Technical Guide*, 2nd ed.; ASM International: Almere, The Netherlands, 2002; pp. 254–283. [CrossRef]
40. Mostafa, A.; Picazo Rubio, I.; Brailovski, V.; Jahazi, M.; Medraj, M. Structure, Texture and Phases in 3D Printed IN718 Alloy Subjected to Homogenization and HIP Treatments. *Metals* **2017**, *7*, 196. [CrossRef]
41. Zhang, D.; Prasad, A.; Bermingham, M.J.; Todaro, C.J.; Benoit, M.J.; Patel, M.N.; Qiu, D.; StJohn, D.H.; Qian, M.; Easton, M.A. Grain Refinement of Alloys in Fusion-Based Additive Manufacturing Processes. *Metall. Mater. Trans. A* **2020**, *51*, 4341–4359. [CrossRef]
42. Sizova, I.; Bambach, M. Hot workability and microstructure evolution of pre-forms for forgings produced by additive manufacturing. *Procedia Eng.* **2017**, *207*, 1170–1175. [CrossRef]
43. Bambach, M.; Sizova, I.; Silze, F.; Schnick, M. Hot workability and microstructure evolution of the nickel-based superalloy Inconel 718 produced by laser metal deposition. *J. Alloys Compd.* **2018**, *740*, 278–287. [CrossRef]
44. Xie, S.; Li, R.; Yuan, T.; Chen, C.; Zhou, K.; Song, B.; Shi, Y. Laser cladding assisted by friction stir processing for preparation of deformed crack-free Ni-Cr-Fe coating with nanostructure. *Opt. Laser Technol.* **2018**, *99*, 374–381. [CrossRef]
45. Santos Macías, J.G.; Elangeswaran, C.; Zhao, L.; Buffière, J.Y.; Van Hooreweder, B.; Simar, A. Fatigue crack nucleation and growth in laser powder bed fusion AlSi10Mg under as built and post-treated conditions. *Mater. Des.* **2021**, *210*, 110084. [CrossRef]
46. Moeini, G.; Sajadifar, S.V.; Engler, T.; Heider, B.; Niendorf, T.; Oechsner, M.; Böhm, S. Effect of Friction Stir Processing on Microstructural, Mechanical, and Corrosion Properties of Al-Si12 Additive Manufactured Components. *Metals* **2020**, *10*, 85. [CrossRef]
47. Chen, X.C.; Shi, C.B.; Guo, H.J.; Wang, F.; Ren, H.; Feng, D. Investigation of Oxide Inclusions and Primary Carbonitrides in Inconel 718 Superalloy Refined through Electroslag Remelting Process. *Metall. Mater. Trans. B* **2012**, *43*, 1596–1607. [CrossRef]
48. Yu, H.; Hayashi, S.; Kakehi, K.; Kuo, Y.L. Study of Formed Oxides in IN718 Alloy during the Fabrication by Selective Laser Melting and Electron Beam Melting. *Metals* **2019**, *9*, 19. [CrossRef]